Observation of Self-Cavitating Envelope Dispersive Shock Waves in Yttrium Iron Garnet Thin Films

P. A. Praveen Janantha,[1] Patrick Sprenger,[2] Mark A. Hoefer,[2] and Mingzhong Wu[1,*]

[1]*Department of Physics, Colorado State University, Fort Collins, Colorado 80523, USA*
[2]*Department of Applied Mathematics, University of Colorado, Boulder, Colorado 80309, USA*
(Received 27 October 2016; published 14 July 2017)

The formation and properties of envelope dispersive shock wave (DSW) excitations from repulsive nonlinear waves in a magnetic film are studied. Experiments involve the excitation of a spin wave step pulse in a low-loss magnetic $Y_3Fe_5O_{12}$ thin film strip, in which the spin wave amplitude increases rapidly, realizing the canonical Riemann problem of shock theory. Under certain conditions, the envelope of the spin wave pulse evolves into a DSW that consists of an expanding train of nonlinear oscillations with amplitudes increasing from front to back, terminated by a black soliton. The onset of DSW self-cavitation, indicated by a point of zero power and a concomitant 180° phase jump, is observed for sufficiently large steps, indicative of the bidirectional dispersive hydrodynamic nature of the DSW. The experimental observations are interpreted with theory and simulations of the nonlinear Schrödinger equation.

In a nonlinear, hydrodynamic medium where dispersion dominates over dissipation, an initial, abrupt increase in a physical quantity (e.g., the water height) can evolve into an expanding waveform composed of a soliton edge followed by diminishing amplitude modulations. Such a nonlinear wave train is called a dispersive shock wave (DSW) [1]. The phenomenon of DSWs is ubiquitous in nature, appearing in dispersive media as diverse as the ocean [2,3], intense laser light [4–6], electron beams [7], ultracold atoms [8–10], and viscous fluids [11]. It is the superfluid or dispersive hydrodynamic analog of a viscous shock wave in a gas [1]. In contrast to the entropy production and energy dissipation due to friction in viscous shock waves, however, a DSW conserves energy, converting the potential energy of an initial jump into the kinetic energy of nonlinear oscillations.

The simplest dispersive hydrodynamics are unidirectional or bidirectional; bidirectional waves correspond to the existence of a fluid velocity in addition to a fluid density and the coexistence of two distinct wave families with different velocities. A universal model of bidirectional dispersive waves is the nonlinear Schrödinger (NLS) equation [1], which can reproduce, for example, the wave function dynamics of a Bose-Einstein condensate [8–10] and the envelope dynamics of light beams in nonlinear media [4–6]. Celebrated features of the NLS model include bright solitons and modulational instability in attractive media [12] and dark solitons and DSWs in repulsive media [13,14]. A canonical, textbook problem in shock wave theory is the Riemann problem, consisting of an initial, steep change in the hydrodynamic medium's thermodynamic variables, e.g., density and velocity [15]. For the repulsive NLS equation, the Riemann problem can result in the generation of an envelope DSW with a dark soliton edge [1,13,14]. Further, the derivative profile of the DSW phase oscillates in tandem with the amplitude. In terms of dispersive hydrodynamics, the square of the DSW amplitude

corresponds to a fluid density, while the phase gradient is analogous to a fluid velocity. A notable property of sufficiently large NLS DSWs is the generation of a zero density (or a vacuum) point with a distinct 180° phase jump. This corresponds to the spontaneous cavitation of a DSW, a property unique to dispersive, *vis-à-vis* viscous, shock waves. What is more, in the reference frame of the dark soliton edge, a cavitating DSW exhibits a surprising feature: the upstream and downstream velocity fields point into the DSW from both sides [1,14]. One can see that the phase plays a rather major role in bidirectional dispersive hydrodynamics in general and self-cavitating DSWs, in particular.

Experimentally, DSWs have been observed in various bidirectional media [4–6,8–10,16,17]. All observations to date, however, have been limited to the evolution of the amplitude (or density) of either localized or periodic pulses, while the phase (or velocity) features have never been studied. In other words, although previous experiments have reported oscillations that appear to go to zero amplitude, they did not measure the phase to make a definitive determination of the self-cavitating signature of DSWs.

This Letter reports the first observation of bona fide self-cavitating envelope DSWs. The experiments use surface spin waves in a $Y_3Fe_5O_{12}$ (YIG) thin film strip that exhibits repulsive nonlinearity and low damping [18], enabling approximate bidirectional dispersive hydrodynamics. The experiments demonstrate envelope DSWs resulting from a step amplitude increase, realizing the dispersive hydrodynamic equivalent of the dam break problem of shallow water theory or, equivalently, the shock tube problem of viscous gas dynamics. Self-cavitation is characterized through both amplitude and phase measurements as well as simulations. The results not only advance the fundamental understanding of DSW physics, but also help interpret various hydrodynamic effects, such as turbulence and decoherence, in

bidirectional nonlinear wave systems including ocean surface waves, optical waves, and spin waves [19–21].

Figure 1(a) depicts the experimental setup. The setup includes a 36.5-mm-long, 1.3-mm-wide YIG thin film strip cut from a YIG wafer grown on a single-crystal $Ga_3Gd_5O_{12}$ substrate via liquid phase epitaxy [22]. The YIG film shows a ferromagnetic resonance linewidth of ∼0.35 Oe at 5 GHz, which corresponds to an effective Gilbert damping constant of ∼9.8×10^{-5}. Two 50-μm-wide, 2-mm-long microstrips are placed above the YIG strip for the excitation and detection of spin waves, and their separation (l) is 20.8 mm. The YIG strip is magnetized to saturation by a magnetic field of 1323 Oe, which is in the YIG plane and perpendicular to the YIG strip length. This film-field configuration supports the propagation of surface spin waves [23–25] with repulsive nonlinearity [18]. For the DSW measurements, the excitation transducer is fed with a microwave step pulse whose power is P_1 just before the step and P_2 just after. Such a microwave pulse excites a spin wave step in the YIG. During the measurements, P_1 and P_2 are varied over 1 μW − 80 mW, but the carrier frequency f_0 is fixed to 6.045 GHz.

Figures 1(b), 1(c), and 1(d) show the characteristics of the device in Fig. 1(a). Figure 1(b) presents the amplitude of the transmission coefficient $\mathbf{S}_{21}$ measured at a microwave power of 20 μW over a frequency (f) range of 5.75–6.30 GHz. In Fig. 1(c), the blue curve presents the spin wave dispersion curve determined from the phase of $\mathbf{S}_{21}(f)$, $\phi(f)$, while the red curve shows a fit. To obtain the experimental curve, the spin-wave wave number $k(f)$ was calculated from $\phi(f)$, using $\phi(f) = k(f)l + \phi_0$

(ϕ_0, a phase constant) and taking $k = 0$ at the low cutoff frequency $f_{\text{cut}} = 5.792$ GHz of the transmission. The fitting used [18,24]

$$2\pi f = |\gamma|\sqrt{H_0(H_0 + 4\pi M_s) + \left(\frac{1}{2}4\pi M_s\right)^2(1 - e^{-2kd})},$$

(1)

where $|\gamma|$ is the gyromagnetic ratio, H_0 is the field, $4\pi M_s$ is the magnetization of the YIG, and d is the YIG film thickness. The horizontal dotted and dashed lines in Figs. 1(b) and 1(c) indicate f_0 and f_{cut}, respectively. Figure 1(d) gives the output power as a function of the input power measured at f_0. The shaded area indicates the P_2 range in which pronounced DSWs were observed.

The data in Fig. 1(b) indicate a spin wave passband of 5.79–6.20 GHz, in which f_0 is centrally located. The transmission profile is relatively smooth, indicating that the spins on the YIG film surfaces are unpinned and a repulsive nonlinearity is expected for the entire frequency range. In films with pinned surface spins, the nonlinearity is repulsive only in narrow frequency ranges [26,27]. The fit in Fig. 1(c) is nearly perfect and yields $|\gamma| = 2.88$ MHz/Oe, $4\pi M_s = 1870$ G, and $d = 11.0$ μm. The $4\pi M_s$ value is slightly larger than the bulk value, mainly due to the assumption of a zero anisotropy field in Eq. (1). The dispersive characteristics of a wave are determined by the dispersion coefficient $D = [\partial^2(2\pi f)/\partial k^2]$. Using the experimental curve in Fig. 1(c), one obtains $D = -11.8 \times 10^3$ cm^2/(rad s) at $f_0 = 6.045$ GHz, very close to the theoretically calculated value -11.3×10^3 cm^2/(rad s). The data in Fig. 1(d) indicate that the spin wave is linearly damped in the $10^{-4} - 1$ mW input power range but is nonlinearly damped for powers larger than 10 mW. This nonlinearity derives mainly from four-wave interactions [12,28].

The DSW data are presented in Figs. 2–5. Figure 2 depicts the main results. Figures 2(a) and 2(b) present the
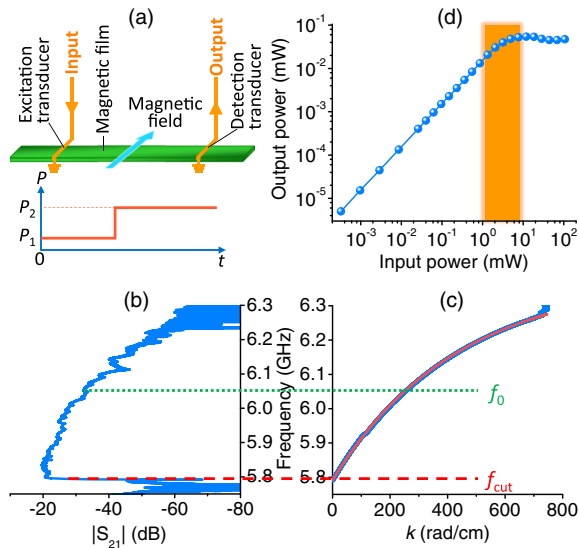
FIG. 1. *Experimental configuration and spin-wave characteristics.* (a) Schematic of the experimental setup. (b) Transmission response of the YIG film strip measured at an input power of $P = 20$ μW. (c) Experimental (blue) and theoretical (red) dispersion curves of spin waves in the YIG film strip. (d) Output power of the YIG film strip device measured as a function of P at 6.045 GHz.
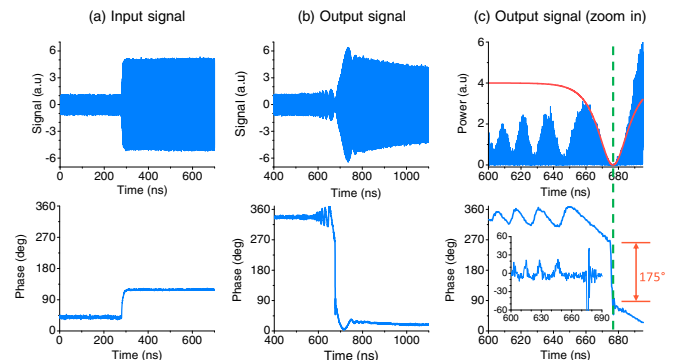
FIG. 2. *Demonstration of a cavitating envelope DSW.* (a) Input signal: top—amplitude; bottom—phase. (b) Output signal: top—amplitude; bottom—phase. (c) Zoom-in display of the output signal shown in (b): top—power (amplitude square); bottom—phase; insert—phase derivative (degree/ns). The red curve in (c) shows a numerical fit to a black soliton profile.

input and output signals, respectively. In each column, the top and bottom panels present the amplitude and phase profiles, respectively. The phase profiles are relative to that of a continuous wave with $f_0 = 6.045$ GHz. In Fig. 2(c), the top panel shows the square of the amplitude data in Fig. 2(b), and the bottom shows the same phase data in Fig. 2(b). The red curve in Fig. 2(c) shows a fit to the square of a black soliton profile [12]

$$u(t) = u_0 \sqrt{1 - \mathrm{sech}^2 \left(u_0 v_g \sqrt{\frac{N}{D}}(t - t_0) \right)}, \qquad (2)$$

where u denotes the spin wave amplitude, u_0 is the black soliton background amplitude, $v_g = \partial(2\pi f)/\partial k$ is the group velocity, $N = \partial(2\pi f)/\partial(|u|^2)$ is the nonlinearity coefficient [18], and t_0 is a time constant. Calculations using the experimental parameters yielded $v_g = 5.0 \times 10^6$ cm/s and $N = -7.7 \times 10^9$ rad/s. u_0 and t_0 are fitting parameters, equal to 3.28×10^{-2} and 277 ns, respectively, for the fit in Fig. 2(c). All the data were taken with $P_1 = 0.14$ mW and $P_2 = 3.47$ mW.

The data in Fig. 2 indicate that an envelope DSW is formed consisting of a train of dark solitonlike dips, with broadening widths from small-amplitude oscillations to termination at a black solitonlike envelope. The observed trailing edge oscillation has almost zero amplitude at its center, a 175° phase jump, and a profile that can be fitted with Eq. (2). The fact that the DSW is terminated by a near 180° phase jump and a black solitonlike oscillation indicates self-cavitation and the formation of a vacuum point where the phase gradient is theoretically infinite [14]. Although this solitonlike oscillation clearly exhibits nonlinear character, the modeling, discussed later, predicts that the DSW has not yet reached its long-time, steady configuration. In the insert, the derivative of the phase profile shows an oscillation behavior, with both the oscillation period and amplitude increasing from the front to the back. Note that the derivative at the oscillation center is beyond the vertical scale and the oscillation reverses polarity, indicative of a vacuum point. Following the DSW is a rarefaction wave (RW), a smooth, expansion wave exhibiting weak oscillations in both amplitude and phase [8]. The long-time evolution of an initial step in the amplitude for the NLS model has been classified [14], resulting in a DSW connected to a RW by an intermediate state. According to the classification and the experimental parameters here, one can expect a faster DSW followed by a slower RW. This prediction is evident in Fig. 2. The phase in Fig. 2(b) reveals an approximately constant, negative slope for the RW. This frequency shift is due to nonlinear dispersion and corresponds to a concomitant positive k shift, as expected by the initial step that maintains a constant frequency.

Figures 3 and 4 present data revealing that DSW formation is sensitive to the characteristics of the initial step. Figure 3 presents data measured with $P_2 = 3.47$ mW while the ratio P_2/P_1 ranges from 1.6 to 50. As P_2/P_1 is increased, the soliton
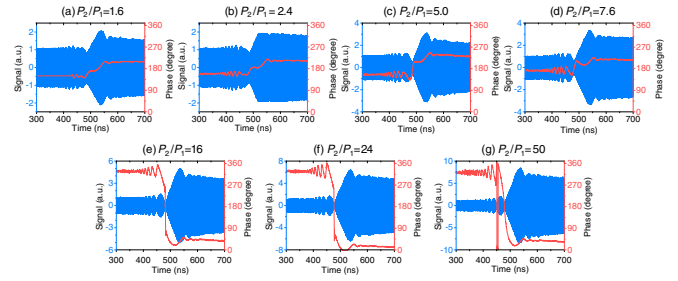

FIG. 3. *Dependence of DSW formation on P_2/P_1.* In each diagram, the signal is shown in blue while the phase is shown in red; P_2/P_1 is indicated on the top. For all the measurements, P_2 was fixed at 3.47 mW.

dip at the DSW edge deepens, with a gray solitonlike dip for P_2/P_1 up to 7.6. A black solitonlike edge and a corresponding vacuum point appear for $P_2/P_1 = 16$, consistent with theory that predicts self-cavitation for $P_2/P_1 > 9$ [1,14]. Higher P_2/P_1 leads to the migration of the vacuum point away from the soliton edge and into the DSW interior, which can be seen, e.g., in Fig. 3(g) where the sharpest phase jump now occurs at the secondary DSW oscillation, again consistent with theory [1,14]. In contrast to the DSW, the phase profile of the RW remains relatively unchanged with increasing P_2/P_1, indicating that the concomitant oscillations are weak and essentially linear. As P_2/P_1 is increased, the DSW amplitude relative to the RW amplitude is reduced, also expected. Therefore, the amplitude of the jump is important for DSW development, deriving from the fact that at the jump, both v_g and D vary due to a nonlinearity-induced dispersion shift. In addition, one can also see that the DSW oscillation shown in Fig. 3(e) has an average frequency of about 68 MHz, while that in Fig. 3(f) has an average frequency of about 65 MHz. This observation agrees qualitatively with the theoretical expectation that the average oscillation frequency of the DSW scales with power. Note that when P_2/P_1 was increased from 16 to 24, P_2 was kept constant while P_1 was decreased.

Figure 4 shows data measured when P_1 and P_2 were increased but P_2/P_1 was kept constant at ~24. The low-power case in Fig. 4(a) lacks the large-amplitude modulation and phase coherence typical of DSWs, while the other cases in Figs. 4(b)–4(e) exhibit nonlinear effects such as increasing amplitude modulations, large phase gradients, and vacuum points. This indicates that nonlinearity is a prerequisite for DSW formation. Figures 4(d) and 4(e) exhibit complex dynamics that deviate from the NLS predictions, likely due to higher-order nonlinear processes.

Figure 5 presents data measured at different positions (x) along the YIG strip, revealing DSW development. In contrast to those presented in Figs. 1–4, these data were obtained using an inductive probe [29,30], not a microstrip. For maximum resolution, the figure limits the presentation to the modulations associated with the DSW, neglecting the accompanying RW. The data indicate how an initial step develops into a DSW, revealing the expanding nature of DSWs in contrast to
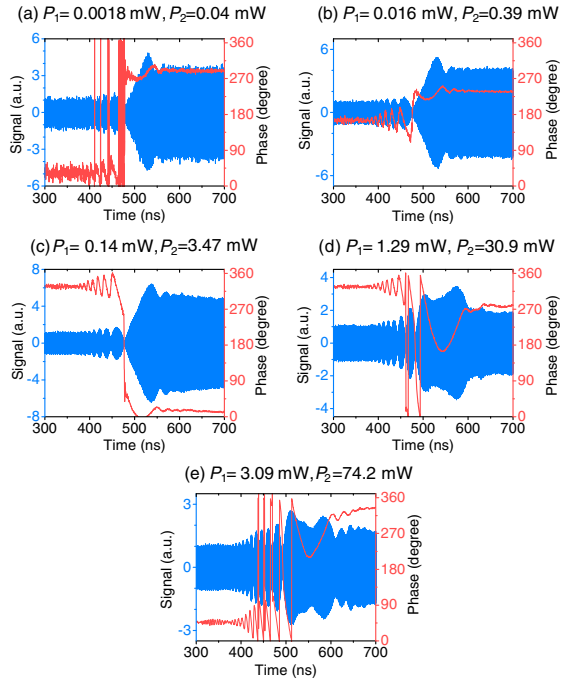
FIG. 4. *Dependence of DSW formation on P_1 and P_2.* In each diagram, the signal is shown in blue while the phase is shown in red; the input power levels are indicated on the top. For all the measurements, P_2/P_1 was kept constant at 24.

the sharp transition in viscous shocks. The fact that DSW formation requires sufficient propagation length is because nonlinearity requires certain propagation time to develop [31,32]. Different from the black solitonlike oscillations in Figs. 2–4, the oscillations in Fig. 5 do not show nearly zero intensity at their centers. This is mainly because the propagation distance for the data in Fig. 5 is much shorter than that for the data in Figs. 2–4, while self-cavitation requires a sufficient propagation distance, as demonstrated by the simulations. Note that the inductive probe has a lower
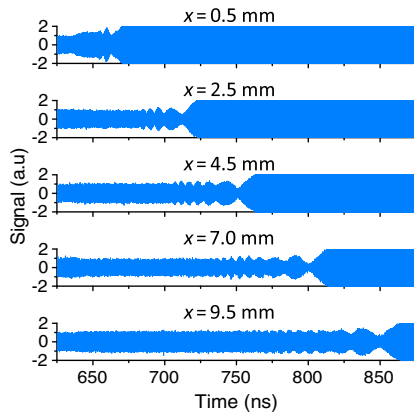
sensitivity than the microstrip transducer and therefore yields noisy signals when $x \geq 20$ mm.

The experimental observations are reproduced by simulations using the NLS equation with damping. Simulations utilized the parameters associated with the experiments and a fitted initial wave amplitude as the spin wave power cannot be precisely determined. The simulation details are given in the Supplemental Material [33], while the main results are featured in Fig. 6. The signals in Fig. 6(a) demonstrate the spatial development of the DSW, which is consistent with that in Fig. 5. The rapid transition time (3 ns) for the initial step results in a Gibbs-type phenomenon [34] with two essentially linear wave packets at short distances (1.9 mm). At 10.4 mm, nonlinearity enhances the lower wave packet resulting in a DSW, while the amplitude of the upper wave packet rarefies into a RW. Consequently, one can trace the weak RW oscillations observed to the rapid step transition. At the output transducer (20.8 mm), the DSW exhibits a vacuum point, which at 101.1 mm has migrated into the interior of the DSW. As shown in Fig. 6(a), the primary role of the damping is to reduce the amplitude by about 20% during the course of propagation. Although not shown in Fig. 6, if a slower step is used, the RW oscillation amplitude is diminished, and DSW development takes longer. This suggests that the experimental observations occur in a transient regime, prior to the long-time regime where the solution to the step problem reaches a fully developed state [14]. Then the DSW trailing edge has not yet reached its long-time, solitonic character. The fact that the experiment does not clearly show the predicted intermediate state, which is expected to occur at an intensity of 2.9 in Fig. 2(b), results from a relatively short evolution distance as well as higher-order nonlinearity [35,36] and nonlinear damping [35,37,38] that are neglected in the simulations. Figure 6(b) presents the amplitude and phase results at $x = 20.8$ mm, while Fig. 6(c) presents the same data but over a narrower time scale. In Fig. 6(b), the DSW is observed followed by an intermediate
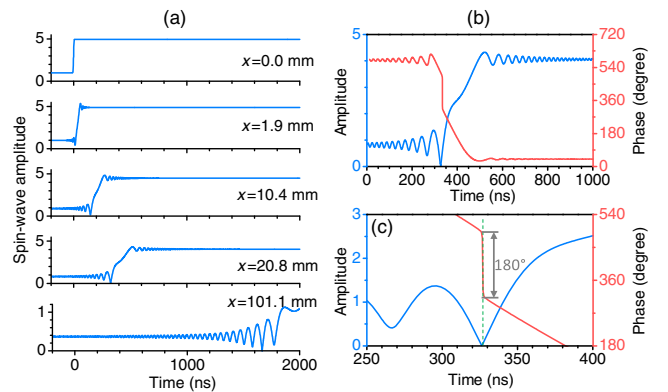

FIG. 5. *Spatial development of DSW.* Each diagram shows the spin wave signal measured by an inductive probe at a distance of x away from the excitation transducer. The measurements were conducted at $P_1 = 0.14$ mW and $P_2 = 3.47$ mW.

FIG. 6. Simulation results. (a) Signals measured at different positions. (b) Amplitude (blue, left axis) and phase (red, right axis) profiles of the signal measured at $x = 20.8$ mm. (c) The same data as in (b) in a narrower time window.

transition state. The RW follows with decreasing oscillations that result from the sharp Riemann problem. One can see a remarkable similarity between the results in Figs. 6(b) and 6(c) and Figs. 2(b) and 2(c), supporting the interpretation of the experimental observations.

In summary, this work demonstrates self-cavitating envelope DSWs for spin waves. The DSW consists of a train of dark solitonlike dips with depths increasing from front to back, terminated by a black solitonlike oscillation. DSW formation is sensitive to the characteristics of the initial spin wave step. A sufficient propagation distance is required for the initial step to evolve into a DSW. Future studies include the exploration of the entire NLS phase diagram for the Riemann problem, DSW-RW interactions, and DSW-soliton interactions. Note that during the revision of this Letter, the development of self-cavitating DSWs was also reported for light waves [39].

---

*Corresponding author.
mwu@colostate.edu

[1] G. A. El and M. A. Hoefer, Physica (Amsterdam) **333D**, 11 (2016).

[2] T. Talipova, E. Pelinovsky, O. Kurkina, and A. Kurkin, Shock and Vibration, **7** 875619 (2015).

[3] S. Trillo, G. Deng, G. Biondini, M. Klein, G. F. Clauss, A. Chabchoub, and M. Onorato, Phys. Rev. Lett. **117**, 144102 (2016).

[4] W. Wan, S. Jia, and J. W. Fleischer, Nat. Phys. **3**, 46 (2007).

[5] J. Fatome, C. Finot, G. Millot, A. Armaroli, and S. Trillo, Phys. Rev. X **4**, 021022 (2014).

[6] C. Conti, A. Fratalocchi, M. Peccianti, G. Ruocco, and S. Trillo, Phys. Rev. Lett. **102**, 083902 (2009).

[7] Y. C. Mo, R. A. Kishek, D. Feldman, I. Haber, and B. Beaudoin, P. G. O'Shea, and J. C. T. Thangaraj, Phys. Rev. Lett. **110**, 084802 (2013).

[8] M. A. Hoefer, M. J. Ablowitz, I. Coddington, E. A. Cornell, P. Engels, and V. Schweikhard, Phys. Rev. A **74**, 023623 (2006).

[9] J. J. Chang, P. Engels, and M. A. Hoefer, Phys. Rev. Lett. **101**, 170404 (2008).

[10] Z. Dutton, M. Budde, C. Slowe, and L. V. Hau, Science **293**, 663 (2001).

[11] M. D. Maiden, N. K. Lowman, D. V. Anderson, M. E. Schubert, and M. A. Hoefer, Phys. Rev. Lett. **116**, 174501 (2016).

[12] M. Remoissenet, Waves Called Solitons: Concepts and Experiments (Springer, Berlin, 1999).

[13] A. V. Gurevich and A. L. Krylov, Sov. Phys. JETP **65**, 944 (1987).

[14] G. A. El, V. V. Geogjaev, A. V. Gurevich, and A. L. Krylov, Physica (Amsterdam) **87D**, 186 (1995).

[15] G. B. Whitham, Linear and Nonlinear Waves (Wiley, New York, 1974).

[16] J. E. Rothenberg and D. Grischkowsky, Phys. Rev. Lett. **62**, 531 (1989).

[17] C. Conti, A. Fratalocchi, M. Peccianti, G. Ruocco, and S. Trillo, Phys. Rev. Lett. **102**, 083902 (2009).

[18] M. Wu, in Nonlinear Spin Waves in Magnetic Film Feedback Rings, edited by Robert Camley and Robert Stamps, Solid State Physics Vol. 62, (Academic Press, Burlington, 2011), p. 163.

[19] E. G. Turitsyna, S. V. Smirnov, S. Sugavanam, N. Tarasov, X. Shu, S. A. Babin, E. V. Podivilov, D. V. Churkin, G. Falkovich, and S. K. Turitsyn, Nat. Photonics **7**, 783 (2013).

[20] A. Costa, A. R. Osborne, D. T. Resio, S. Alessio, E. Chrivi, E. Saggese, K. Bellomo, and C. E. Long, Phys. Rev. Lett. **113**, 108501 (2014).

[21] S. Randoux, P. Walczak, M. Onorato, and P. Suret, Phys. Rev. Lett. **113**, 113902 (2014).

[22] R. C. Linares, J. Cryst. Growth **3**, 443 (1968).

[23] P. Kabos and V. S. Stalmachov, Magnetostatic Waves and Their Applications (Chapman and Hall, London, UK, 1994).

[24] D. D. Stancil and A. Prabhakar, Spin Waves—Theory and Applications (Springer, New York, 2009).

[25] S. O. Demokritov, B. Hillebrands, and A. N. Slavin, Phys. Rep. **348**, 441 (2001).

[26] B. A. Kalinikos and A. N. Slavin, J. Phys. C **19**, 7013 (1986).

[27] B. A. Kalinikos, N. G. Kovshikov, and A. N. Slavin, Zh. Eksp. Teor. Fiz. **94**, 159 (1988) [Sov. Phys. JETP **67**, 303 (1988)].

[28] A. D. Boardman and S. A. Nikitov, Phys. Rev. B **38**, 11444 (1988).

[29] M. Wu, M. A. Kraemer, M. M. Scott, C. E. Patton, and B. A. Kalinikos, Phys. Rev. B **70**, 054402 (2004).

[30] K. R. Smith, M. J. Kabatek, P. Krivosik, and M. Wu, J. Appl. Phys. **104**, 043911 (2008).

[31] N. G. Kovshikov, B. A. Kalinikos, C. E. Patton, E. S. Wright, and J. M. Nash, Phys. Rev. B **54**, 15210 (1996).

[32] M. Chen, M. A. Tsankov, J. M. Nash, and C. E. Patton, Phys. Rev. B **49**, 12773 (1994).

[33] See Supplemental Material at http://link.aps.org/supplemental/10.1103/PhysRevLett.119.024101 for a description of the NLS modeling and numerical computations.

[34] J. C. DiFranco and K. T. McLaughlin, Int. Math. Res. Pap. **8**, 403 (2005).

[35] Z. Wang, M. Cherkasskii, B. A. Kalinikos, L. D. Carr, and M. Wu, New J. Phys. **16**, 053048 (2014).

[36] J. Q. Anderson, R. A. Ryan, M. Wu, and L. Carr, New J. Phys. **16**, 023025 (2014).

[37] M. M. Scott, C. E. Patton, M. P. Kostylev, and B. A. Kalinikos, J. Appl. Phys. **95**, 6294 (2004).

[38] Z. Wang, M. Cherkasskii, B. A. Kalinikos, and M. Wu, Phys. Rev. B **91**, 174418 (2015).

[39] G. Xu, M. Conforti, A. Kudlinski, A. Mussot, and S. Trillo, [Phys. Rev. Lett. (to be published)].